RESEARCH

Unveiling ac4C modification pattern: a prospective target for improving the response to immunotherapeutic strategies in melanoma

Jianlan Liu[1†], Pengpeng Zhang[2†], Chaoqin Wu[1†], Binlin Luo[3*], Xiaojian Cao[1*] and Jian Tang[3*]

Abstract

Emerging evidence has confirmed the inextricable connection between N4-acetylcytidine (ac4C) mRNA modification and the clinical characteristics of malignancies. Nonetheless, it is uncertain whether and how ac4C mRNA modification patterns affect clinical outcomes in melanoma patients. This research integrated single-cell sequencing data and transcriptomics to pinpoint ac4C-related genes (acRG) linked to melanoma progression and evaluate their clinical implications. Cells with elevated acRG score were predominantly located within the melanocytes cluster. Intercellular communications between melanocytes and other cell subtypes were markedly strengthened in the acRG-high group. We developed and confirmed an excellent acRG-related signature (acRGS) utilizing a comprehensive set of 101 algorithm combinations derived from 10 machine learning algorithms. Hereby, the acRGS, including MYO10, ZNF667, MRAS, SCO2, MAPK10, PNMA6A, KPNA2, NT5DC2, BAIAP2L2 and NDST3, delineated ac4C-associated mRNA modification patterns in melanoma. The acRGS possesses distinctly superior performance to 120 previously reported signatures in melanoma and could predict the overall survival of melanoma patients across four external datasets. The substantial associations among immune checkpoint genes, immune cell infiltration, and tumor mutation burden with acRGS indicate that acRGS is helpful in identifying melanoma patients who are sensitive to immunotherapy. Besides, we confirmed that MYO10 was mainly overexpressed in melanoma tissues, and elevated MYO10 was positively correlated with malignant phenotypes and unfavorable prognosis in melanoma patients. Silencing MYO10 expression inhibited melanoma cell proliferation, migration and invasion in vitro as well as tumor growth in vivo. Taken together, the acRGS could function as a reliable and prospective tool to improve the clinical prognosis for melanoma individuals.

†Jianlan Liu, Pengpeng Zhang and Chaoqin Wu have contributed equally to this work and share first authorship.

*Correspondence:
Binlin Luo
luobin8212192340@sina.com
Xiaojian Cao
xiaojiancao001@163.com
Jian Tang
tangjian@njmu.edu.cn

Full list of author information is available at the end of the article

Introduction

Melanoma, characterized by significant heterogeneity and aggressiveness, is highly prevalent and lethal due to its strong metastatic potential, frequently spreading to sentinel lymph nodes, nearby subcutaneous tissues, and distant organs such as the lungs, brain, and liver [1, 2]. Melanoma is categorized into four primary subtypes: cutaneous melanomas without chronic sun-induced damage; cutaneous melanomas with chronic sun-induced damage; mucosal melanomas; acral melanomas [3]. The therapeutic strategies used to manage advanced acral melanoma are the same as cutaneous melanoma in clinical practice. Over the past decade, therapeutic strategies for melanoma have advanced considerably with the innovations of molecular targeted medicines and immunotherapies. Notably, patients suffering from advanced BRAF^{V600}-mutant melanoma exhibit a positive response to combination BRAF/MEK inhibitors, with a median overall survival (OS) prolongation of 5–17 months as opposed to the BRAF inhibitor vemurafenib alone [4, 5]. Immunotherapies targeting the immunological inhibitory receptors, such as cytotoxic T-lymphocyte antigen 4 (CTLA-4) and programmed cell death 1 (PD-1), boost the immune reactions mediated by T cell and significantly improve patient outcomes [6]. However, both molecular targeted therapies and immunotherapies face challenges due to the emergence of drug resistance and associated toxicities. Combination therapies, in particular, often lead to more severe toxicities, frequently necessitating treatment discontinuation [7, 8]. Crucially, the mechanisms of drug resistance are frequently variable both within patients and individual tumors, demonstrating that such heterogeneity could contribute to adverse treatment response and therapeutic failure [4]. Accordingly, there is an urgent need to clarify melanoma heterogeneity, recognize patients who are sensitive to immunotherapies or molecular targeted therapies, develop effective and novel biomarkers, and ultimately improve clinical outcomes in melanoma.

RNA modifications, including N6 methyladenosine, pseudouridine, 5-methylcytidine, and N4-acetylcytidine (ac4C), are regulated by specific "writers" and "erasers", allowing for dynamic changes that influence various physiological and pathological processes through "reader" proteins [9, 10]. Among these modifications, ac4C has recently been characterized as an mRNA modification that plays critical functions in mRNA stability and translation. Initially, it appeared in bacterial transfer RNA (tRNA) anticodons and later in eukaryotic serine and leucine tRNAs as well as 18 S ribosomal RNA (rRNA) [11, 12]. Acetylation as the N4 position of cytosine is mediated by the ac4C "writer", with N-acetyltransferase 10 (NAT10) currently determined as the exclusive enzyme accountable for this modification [11]. There has been an increasing focus on the regulatory functions of ac4C modification in diverse cancer types [11]. Numerous studies have elucidated the molecular mechanisms linking ac4C modification to cancer progression, encompassing critical aspects such as cell proliferation, metastasis, metabolism, and resistance to chemotherapy [13–15]. Given the distinct expression of ac4C modification in disease and cancer detection, along with its critical impact on cancer development, targeting ac4C modification has become a promising strategy for cancer detection and treatment [16, 17]. However, limited research has explored the link between ac4C modification to the biological process of melanoma, which remains an area of significant interest. Therefore, further investigations are necessary to understand the impact of ac4C modification in melanoma diagnosis and therapy.

In this study, we performed extensive investigations about ac4C modification in melanoma, utilizing advanced bioinformatics techniques to assess its levels in mRNA. Single-cell RNA sequencing (scRNA-seq), integrated with multi-omics approaches, was employed to offer a detailed characterization of the cellular landscape in melanoma patients. This approach allowed for the exploration of the relationship between various cell subtypes and ac4C modification activity. Based on differentially expressed genes (DEGs) among cell subgroups, we developed a prognostic model using ten machine learning (ML) algorithms, which demonstrated superior accuracy compared to existing models, underscoring its potential clinical utility. Functionally, we evaluated the potential of predictive models to identify melanoma patients who respond to immunotherapy by analyzing the dynamic interactions among immune components in melanoma. Additionally, we conducted a series of experiments to explore the biological functions of MYO10, a crucial gene identified in our model, in melanoma progression. Collectively, this work provides innovative perspectives into the application of ac4C modification in melanoma, paving the way for individualized therapeutic approaches and improved clinical effects for melanoma patients.

Materials and methods

Data availability

ScRNA-seq data specific to melanoma were accessible in the Gene Expression Omnibus (GEO) database (https://www.ncbi.nlm.nih.gov/geo/) with accession number GSE215120 [18]. This dataset included five acral

melanoma and three cutaneous melanoma samples for subsequent analysis. Bulk RNA sequencing data and clinical data of melanoma were sourced from The Cancer Genome Atlas (TCGA) via UCSC Xena (https://tcga.xenahubs.net), while gene expression profiles for normal skin tissue were retrieved from the Genotype-Tissue Expression (GTEX, https://gtexportal.org/) databases. Following standardization, samples without survival data were excluded, resulting in 470 melanoma samples and 810 normal skin samples. Additionally, gene expression matrices from GSE19234, GSE53118, and GSE54467 were acquired from GEO for further analysis [19–21]. To guarantee consistency and comparability, gene expression data were standardized to transcripts per million (TPM), and batch effects were corrected through the "combat" function from the "sva" package [22]. Principal component analysis (PCA) was conducted to confirm the successful batch correction. All datasets from TCGA and GEO were log-transformed at the beginning of the analysis to ensure standardization. Recent studies have revealed that NAT10 acetylates mRNA, contributing valuable insights into epitranscriptome. In particular, ac4C RNA immunoprecipitation sequencing (ac4C-RIP-seq) performed on wild-type and NAT10-deficient HeLa cells identified 2,135 genes influenced by NAT10-driven ac4C modification, collectively referred to as the ac4C-related gene set (acRG) [9]. Gene lists were summarized in Table S1.

Cell subtype classification and annotation in melanoma

scRNA-seq uncovers the diversity and complexity of single-cell transcriptomes, mapping cell type composition and intercellular communication across samples. Following quality control and normalization, cells with fewer than 300 detected genes or above 10% mitochondria genes were eliminated to avoid analytical bias. Potential doublet cells were removed using the DoubletFinder program. Batch effects were corrected through canonical correlation analysis, which identified "anchors" between different batches. After cell clustering with the "FindClusters" function at a resolution of 0.5, the results were visualized using uniform manifold approximation and projection (UMAP). Positive marker genes for each cluster were determined employing the "FindAllMarkers" function. Subsequently, dotplots were generated to illustrate the expression patterns of marker genes across subgroups. Cell clusters were categorized with respect to DEGs and known markers from published research. The proportion of cell types was visualized using UMAP. Enrichment analysis of DEGs was conducted using the "clusterprofiler" program to investigate cell type functions. Clusters were enriched for gene ontology (GO) biological process (BP) and Kyoto Encyclopedia of Genes

and Genomes (KEGG) pathways, with statistical significance established at an adjusted P-value < 0.05.

Scoring of acRG activity among different cell types

To quantify the activity of the acRG across different cell types, we implemented five scoring approaches: AUCell, singscore, UCell, ssGSEA and AddModuleScore [23]. These methods aimed to characterize the intrinsic connections among cell types, states and active biological processes. Cells with high acRG expression were assigned higher scores, which were then projected onto UMAP and color-coded to highlight the clusters where acRG activity was most prominent.

Cell-cell interaction analysis

Next, we employed the "cellchat" package [24] to deduce, analyze, and depict receptor-ligand signaling interactions between acRG-high and acRG-low groups. This analysis clarified the contributions of acRG groups to specific signaling pathways. Interaction numbers and weights provide the basis for the construction of aggregated cell-cell communication networks.

Identification of critical genes

We adopted the "FindMarker" function to recognize genes with considerable variations between acRG-high and acRG-low groups, with a fold change > 1.5 considered significant. Besides, the top 150 genes with the highest connections with acRG score were screened utilizing spearman correlation analysis and merged them with the previously significant DEGs for constructing predictive models.

Generation of acRG-related signature using machine learning

Prior to formal model construction, we employed the "survival" R package and univariate COX regression analysis to ascertain significant predictive genes. Subsequently, to develop a highly accurate and stable predictive model, we incorporated 10 ML techniques and 101 algorithm permutations, including random survival forest (RSF), stepwise Cox, elastic network (Enet), Cox Boost, supervised principal components (SuperPC), Lasso, partial least squares regression for Cox (plsRcox), Ridge, generalized boosted regression modeling (GBM), and survival support vector machine (survival-SVM) [25, 26]. The analytical process is as follows: (a) identifying prognostic biomarkers through univariate Cox regression; (b) applying 101 algorithm permutations using a leave-one-out cross-validation (LOOCV) framework; (c) validating the model across three independent datasets (GSE19234, GSE53118, GSE54467); and (d) calculating the Harrell's concordance index (C-index) across all validation datasets [26]. The signature exhibiting the highest average

Liu *et al. Journal of Translational Medicine*   (2025) 23:287

Page 4 of 21

C-index was selected as the most effective acRG-related signature (acRGS).

Comparative analysis of acRGS with existing prognostic signatures

To assess the effectiveness of acRGS relative to other signatures, previously published models, including gene coefficients and model effects, were retrieved from the literature (Table S2) [27]. C-index values were then calculated for the TCGA cohort using both acRGS genetic features and those from published models. The results were presented in descending order, with the greatest C-index values listed first.

Validation of prognosis and diagnostic efficacy of acRGS

To verify the robustness and predictive power of acRGS, we employed multifaceted approaches encompassing Kaplan-Meier (KM) analysis, PCA, and receiver operating characteristic (ROC) curve assessment. Patients in the low and high-acRGS cohorts were stratified as defined by median risk scores, with group differences tested via the Log-Rank test. ROC analysis was performed to assess model efficiency, with the area under the curve (AUC) calculated to confirm diagnostic accuracy. Furthermore, PCA was conducted utilizing the 'prcomp' function to evaluate the potential for stratifying patients into two separate groups with regard to their acRGS scores. Finally, we conducted a comparative analysis of the acRGS and clinicopathological features to evaluate the performance of acRGS in predicting the prognosis of melanoma patients.

Characterization of copy number variation and mutations

To investigate the mutation profile of acRGS in melanoma, we employed the "GDCquery" function from the "TCGAbiolinks" R package to obtain simple nucleotide variation data. Recurrent focal genomic regions were determined through the application of the GISTIC 2.0 algorithm (https://gatk.broadinstitute.org). Copy number variation (CNV) events were classified into four categories based on GISTIC amplitude: shallow and deep deletions, as well as different level amplifications. Standardardized tumor mutation burden (TMB) and gene mutation frequencies were then calculated for both acRGS groups. The mutation landscape was visualized with the "maftools" R package [28]. We also investigated the relationship between the acRGS score and TMB. Patients were further stratified into two subgroups depending on median TMB levels, and the disparity in survival rates among these groups was then examined.

Immune infiltration and therapeutic response analysis

To better understand the associations between acRGS and tumor microenvironment (TME), we applied seven algorithms—CIBERSORT, CIBERSORT_abs, QUANTISEQ, MCPcounter, TIMER, EPIC and Xcell—to assess immune cell proportions within melanoma samples. The "estimate" package was utilized to measure immune, stromal, and ESTIMATE scores, providing an extensive investigation of the TME [29]. Furthermore, single-sample gene set enrichment analysis (ssGSEA) was performed to evaluate immune-related pathway activities and infiltration levels. The correlations among immune checkpoint genes (ICGs), hub genes, and immune cell infiltration were explored to elucidate the contributions of these genes to immune functions. To evaluate the predictive potential of acRGS for immunotherapy, we utilized The Cancer Immunome Atlas (TCIA) method to examine its association with therapeutic response and patients' prognosis. Additionally, we also downloaded and analyzed two real-world immunotherapeutic cohorts: the IMvigor210 dataset, which includes the microarray, survival and anti-PD-L1 immunotherapy data of metastatic urothelial cancer patients [30], and GSE78220 cohort comprises transcriptional data for metastatic melanoma patients undergoing anti-PD-1 therapy [31].

Functional annotation of acRGS

Gene set variation analysis (GSVA) utilized the "c2. cp.reactome.v7.4.symbols.gmt" reference to discern signaling pathways and immunomodulatory patterns associated with acRGS. Additionally, GSEA was applied to compare GO and KEGG pathway activation between acRGS groups, uncovering molecular and functional differences that may explain variations in patient outcomes.

Prognosis and drug sensitivity analysis of MYO10 in melanoma

The MYO10 gene, demonstrating the strongest positive correlation with acRGS score for melanoma, was selected as the critical gene in this context. Subsequently, its prognostic relevance, immunological infiltration profile, and pharmacological sensitivity were further examined via the BEST database [32]. Additionally, MYO10 protein levels in melanoma were explored utilizing the Human Protein Atlas (HPA) (http://www.proteinatlas.org/) [33].

Patients and samples

Melanoma patients underwent complete surgical excision of the primary site, with a conclusive pathological diagnosis by two independent pathologists, excluding those who received prior radiation or chemotherapy. Surgically excised melanoma specimens were flash-frozen in liquid nitrogen and then transferred to a -80 °C refrigerator for long-term preservation. All tissue specimens were collected from primary lesions of malignant melanoma patients, as well as normal skin tissue located two

Liu *et al. Journal of Translational Medicine*   (2025) 23:287

Page 5 of 21

centimeters away from the tumor site, rather than from lymph nodes or metastatic lesions. Comprehensive clinicopathological and follow-up data were collected for all participants. The Ethics Committee of the First Affiliated Hospital of Nanjing Medical University approved this study (No. 2022-SR-465), and informed consent was acquired from all patients for sample collection and data preservation.

Construction of MYO10 melanoma knockdown cell line

A375 and SK-Mel-28 (melanoma cell lines), along with HaCaT (human keratinocytes), were obtained from the Cell Bank of the Chinese Academy of Sciences (Shanghai, China). All cells were cultivated in DMEM medium (Gibco, USA) supplemented with 10% fetal bovine serum (FBS) (Gibco, USA), 1% penicillin/streptomycin (Gibco, USA) and kept at 37 °C in a 5% CO_2 incubator. All cells tested negative for mycoplasma. Melanoma cells were inoculated in six-well plates (1.5×10^4 cells per well) and infected with lentivirus (Hanbio, Shanghai, China) carrying short hairpin RNA (shRNA) sequences directed against MYO10 or control shRNA (see Table S3 for details). Stable MYO10 knockdown melanoma cells were achieved by treating with puromycin (1 µg/ml) for one week. The efficacy of MYO10 knockdown was confirmed via quantitative real-time polymerase chain reaction (qRT-PCR) analysis.

RNA extraction and qRT-PCR

Total RNA was extracted from melanoma tissues and cells using TRIzol reagent (Invitrogen, USA) following the manufacturer's guidelines. cDNA was generated with the HiScript III RT SuperMix for quantitative PCR (Vazyme, Nanjing, China). Real-time PCR was conducted utilizing SYBR Green Master Mix (Vazyme, Nanjing, China), with the primer sequences provided in Table S3. The investigation utilized the StepOne Plus Real-Time PCR System (Applied Biosystems, USA), and transcript levels were quantified using the $2^{-\Delta\Delta Ct}$ method.

ac4C RNA Immunoprecipitation (RIP) assay and qRT-PCR

ac4C-RIP was conducted using an RNA immunoprecipitation kit (Genelily Biotech, Shanghai, China) in accordance with the manufacturer's guidelines. Briefly, cells were lysed through 1 mL RIP lysis buffer for 10 min, and then 100 µL of the lysates were stored at -80 °C. An anti-ac4C antibody (Abclonal, Wuhan, China) or normal rabbit IgG (Abclonal, Wuhan, China) was mixed with protein A/G beads at 4 °C for 2 h, followed by incubation with 450 µL of the lysate at 4 °C for 2 h. After washing the beads with buffer, the RNA was extracted, and then qRT-PCR was executed as previously described.

Exploration of the proliferative capacity of melanoma cells after MYO10 knockdown

Melanoma cell viability was determined based on the Cell Counting Kit-8 assay (CCK-8, Yeasen, Shanghai, China). Briefly, cells were inoculated in 96-well plates (2×10^3 cells per well) and incubated with CCK-8 reagent for 1 h at the specified time intervals (0, 24, 48, 72, and 96 h), and absorbance was recorded at 450 nm using a microplate reader (A33978, Thermo, USA). For the colony formation assay, 800 melanoma cells were inoculated into 6-well plates (Corning, NY, USA), with the medium changed every three days until visible colonies formed. Subsequently, cells were cleaned with phosphate buffer saline (PBS), fixed with 4% paraformaldehyde, and colored with 1% crystal violet. Colonies containing over 10 cells were manually enumerated, with results averaged across duplicate wells.

Investigation of melanoma cell migratory and invasiveness following MYO10 knockdown

For invasion assays, 24-well transwell plates (8-µm pore size, Corning, NY, USA) were used. A total of 5×10^4 cells, suspended in serum-free medium, were placed in the upper chambers coated with Matrigel (Yeasen, Shanghai, China). The lower chambers were filled with 0.7 ml of DMEM medium containig 10% FBS. For migration assays, the only difference was the absence of Matrigel in the upper chamber, and the procedure was identical. After incubation for an appropriate duration, the cells were fixed in 4% paraformaldehyde, stained with crystal violet, and counted under a microscope. For wound-healing migration assays, a sterile 200 µl pipette tip was used to create a linear scratch in the cell monolayers. The average distance migrated was measured under a microscope at 0 and 48 h.

Tumor xenograft model in vivo

Four-week-old female BALB/c nude mice were acquired from the GemPharmatech company (Nanjing, China) for tumor xenograft experiments. A375 melanoma cells (2×10^6 cells in 100 µL PBS), stably transfected with either MYO10 or control lentivirus, were injected percutaneously into the mice's axilla to assess tumorigenicity. Tumor weights and volumes were recorded every five days using vernier calipers, and the mice were sacrificed after 25 days. Tumor volume was calculated using the formula: volume = (width^2 × length) / 2. All animal procedures adhered to the ethical guidelines of the Animal Experiments Committee at Nanjing Medical University (IACUC-2403031).

Statistical analysis

Data processing, statistical analysis, and visualization in the bioinformation analysis were implemented using R

software (version.4.2.0). All in vitro tests were conducted at least three times. The data were analyzed utilizing GraphPad Prism 8.0 (GraphPad Software, Inc., USA), and the results are expressed as the mean ± standard deviation (SD). The student's t-test or Tukey's multiple comparisons test was employed for comparisons between two groups, while one-way ANOVA was utilized for comparisons among several groups. All statistical tests were bilateral, and differences were deemed statistically significant at $p < 0.05$.

Results

Analysis at the single-cell level of melanoma

The study workflow is outlined in Fig. 1. After quality control, low-quality cells were excluded, leaving 59,182 cells for analysis, including 33,749 cells from acral melanoma and 25,433 from cutaneous melanoma (Fig. 2A). Following log-normalization and dimensionality reduction, 23 distinct cell subpopulations were identified (Fig. 2B). As per the specific gene expression patterns of these clusters, the cell types were labeled as melanocytes (clusters 0, 1, 2, 4, 7, 9, 10, 13, 17), endothelial cells (clusters 14, 20), fibroblasts (clusters 15, 22), Plasma B cells (cluster 11), T cells (clusters 3, 8 12, 19), smooth muscle cells (clusters 16), macrophages (clusters 18, 21), and NK cells (clusters 5, 6) (Fig. 2C, D). Additionally, the percentage distribution of cell types across each sample was visualized in Fig. 2E. Functional enrichment analysis revealed

significant pathway differences across cell populations (Fig. 2F). Moreover, Fig. 2G shows potential molecular interactions, highlighting the heterogeneity of communication between cell populations. Based on an extensive literature review, 2,135 genes most closely linked to ac4C modification were selected for further analysis. These genes were utilized to assess acRG activity among cell types using five distinct algorithms (Fig. 3A). Cells were separated into acRG-high and acRG-low groups according to median scores (Fig. S1A). As illustrated in Fig. 3B, melanocytes, fibroblasts and endothelial cells exhibited the highest activity, while plasma B cells and T cells showed the lowest, as confirmed by the UMAP plot (Fig. 3D). Additionally, we observed significant differences in cell type composition and distribution between the acRG_high and acRG_low groups, with melanocytes constitute the majority in the acRG_high group (Fig. S1B). Marker genes for both groups were identified, and the major marker genes for each population were depicted using bubble plots (Fig. 3C). Further cell communication analysis demonstrated that the acRG-high group exhibited markedly greater intercellular interactions than the acRG-low group, with melanocytes and fibroblasts being central to communication (Fig. 3E, F). The strength of incoming and outgoing signals was higher in the acRG-high cohort, as illustrated in Figs. 3G and 4A. Finally, the top 150 genes closely correlated with acRG score were selected for further analysis (Fig. 3H).
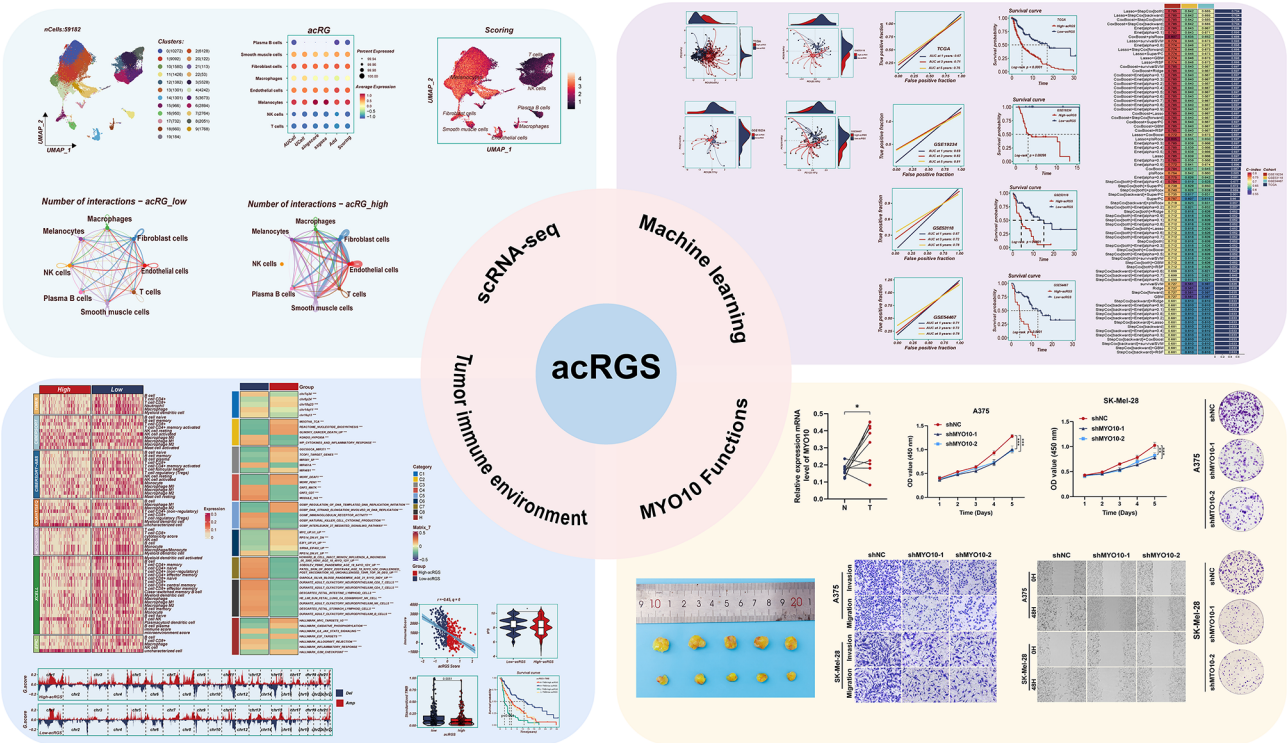

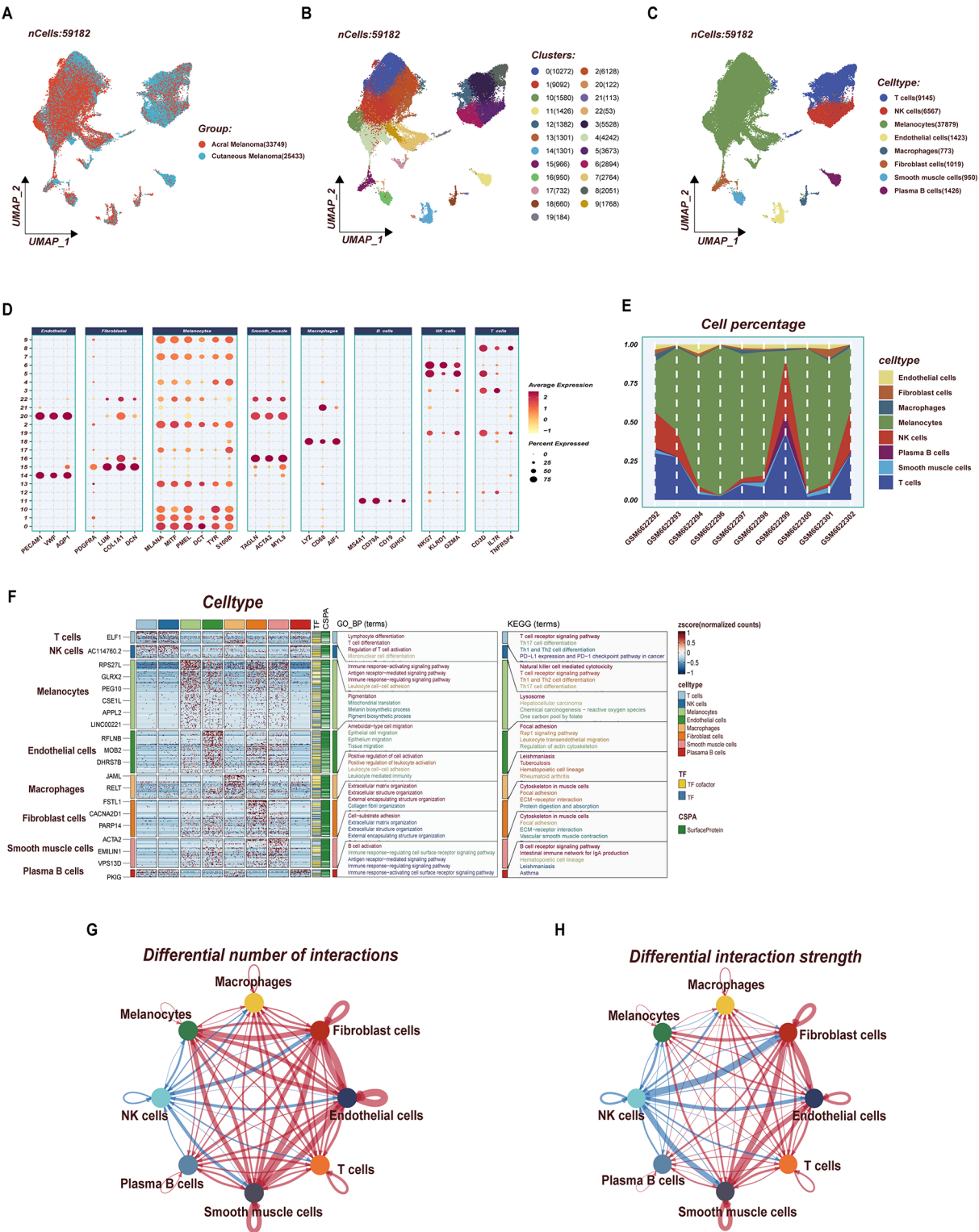**Fig. 1** The detailed research flowchart

Fig. 2 Cell type annotation based on distinct cell markers in melanoma samples. (**A**) A Uniform manifold approximation (UMAP) plot of acral melanoma and cutaneous melanoma is presented. (**B**) UMAP visualization of 23 clusters. (**C**) UMAP visualization of eight cell types, including 9,145 T cells, 6,567 NK cells, 37,879 melanocytes, 1,423 endothelial cells, 773 macrophages, 1,019 fibroblast cells, 950 smooth muscle cells and 1,426 plasma B cells. (**D**) The dot plot illustrates the average and percent expression levels of marker genes across various cell subtypes. (**E**) The line chart displays the distribution of each cell type throughout the samples. (**F**) GO and KEGG enrichment analysis of differentially expressed genes among various cell subtypes. (**G**-**H**) Cellchat analysis of all cell types. Both the numbers of interactions and their respective intensities were demonstrated
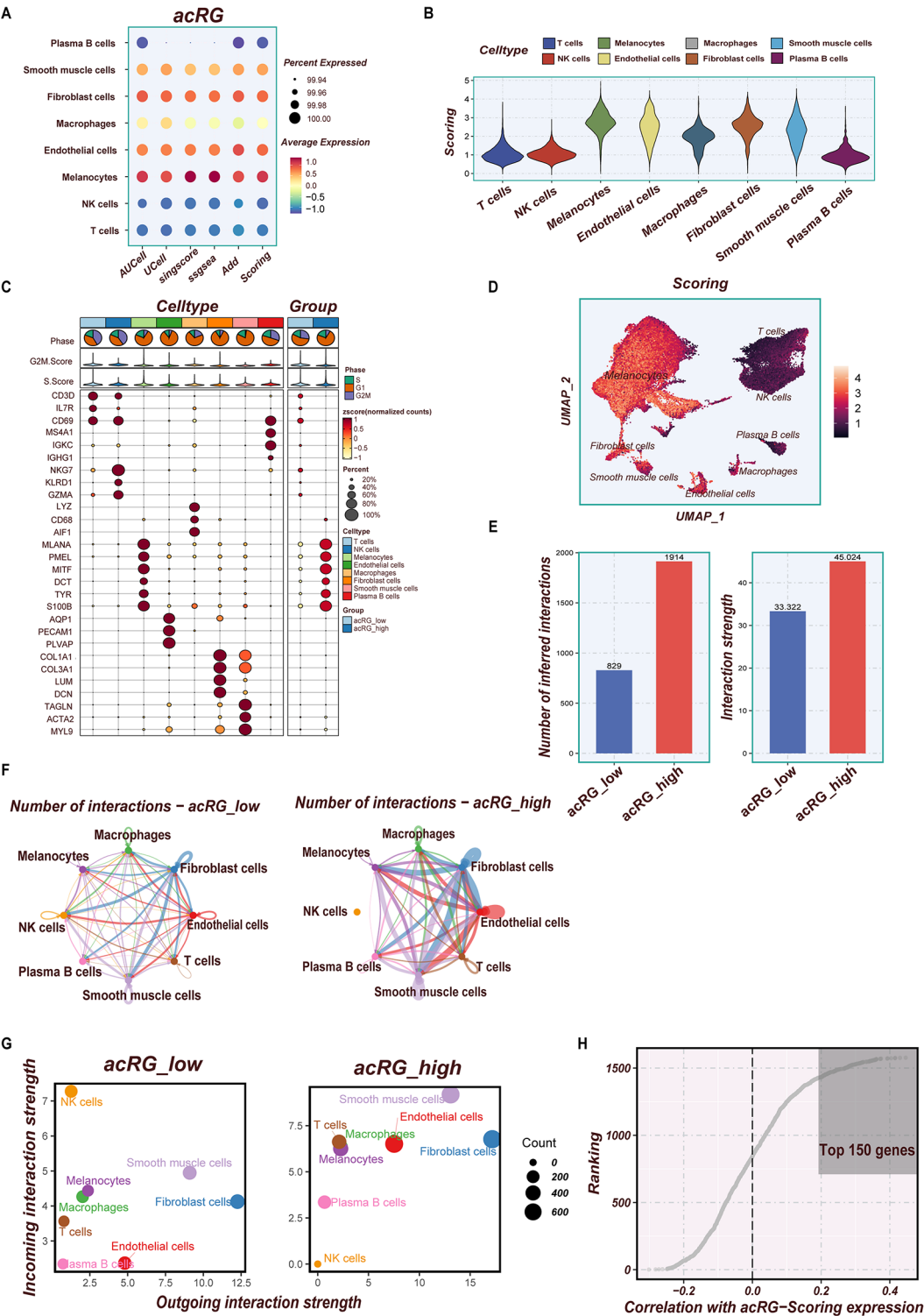
Fig. 3 Evaluation of acRG activity scores in different kinds of cells. (**A**) Bubble plots depict the activity score of acRG across eight cell types implementing AUCell, UCell, singscore, ssGSEA, AddModulescore, and Scoring (the sum of scores from other algorithms). (**B**) Violin plots depict the activity score of acRG across eight cell types implementing Scoring. (**C**) The bubble graphic demonstrates the cell cycle phases and expression of maker genes for eight cell types across two acRG groups. (**D**) The UMAP plot visualizes the acRG activity score in each cell type. (**E**) the bar graph exhibits cellular communication according to the number and strength of interactions. (**F**) Network diagrams demonstrate enhanced intercellular communication in the acRG-high group. (**G**) Comparison of signaling dynamics between acRG-high and acRG-low groups, proving more robust signaling in the acRG-high group. (**H**) Identification of the top 150 genes experiencing the strongest correlations with acRG score
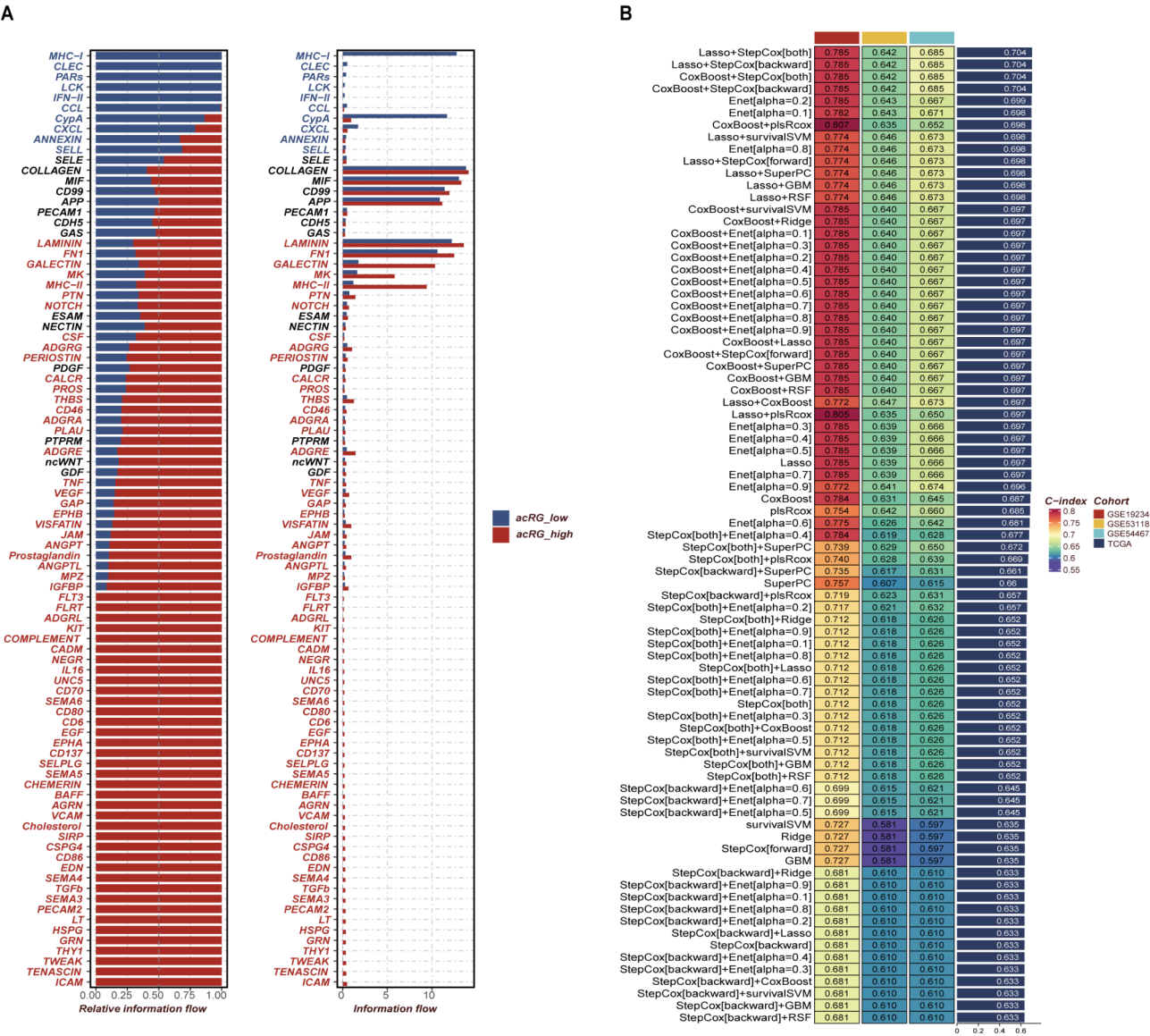
Fig. 4 A prognostic acRGS was developed by applying machine learning algorithms. (**A**) Comparison of the number of signaling pathways between the acRG-high and acRG-low cohorts. (**B**) A total of 101 permutations of machine learning processes were employed to construct acRG-related signatures (acRGS), and the C-index for each model was determined across all validation datasets. The model established through the Lasso + StepCox(both) method is the most effective

Development and evaluation of acRGS

To identify key genes from scRNA-seq analysis, we first intersected the top 150 genes with the previously identified DEGs. K-M analysis and univariate Cox regression yield 43 prognostic genes from the acRG expression patterns. These genes were then subjected to develop a consensus acRGS through an ML-based integrative process. In the TCGA cohort, 101 algorithm combinations were tested using the LOOCV framework to generate acRGS, and the mean C-index for each algorithm was calculated using external validation sets (GSE19234, GSE53118, GSE54467). Notably, the optimal model, combining Lasso and stepwise Cox (direction = both), achieved the

greatest C-index (0.704) and consistently ranked highest across all validation sets (Fig. 4B). Risk scores were calculated for each sample in the training and internal validation sets, with patients separated into high-acRGS and low-acRGS groups with regard to the optimal cut-off value.

Evaluation of acRGS as an independent prognostic indicator for melanoma patients

As shown in Fig. 5A-D, patients in the high-acRGS category had substantially worse OS compared to those in the low-acRGS in both the training dataset and three external validation datasets (*P* < 0.05). ROC curve analysis
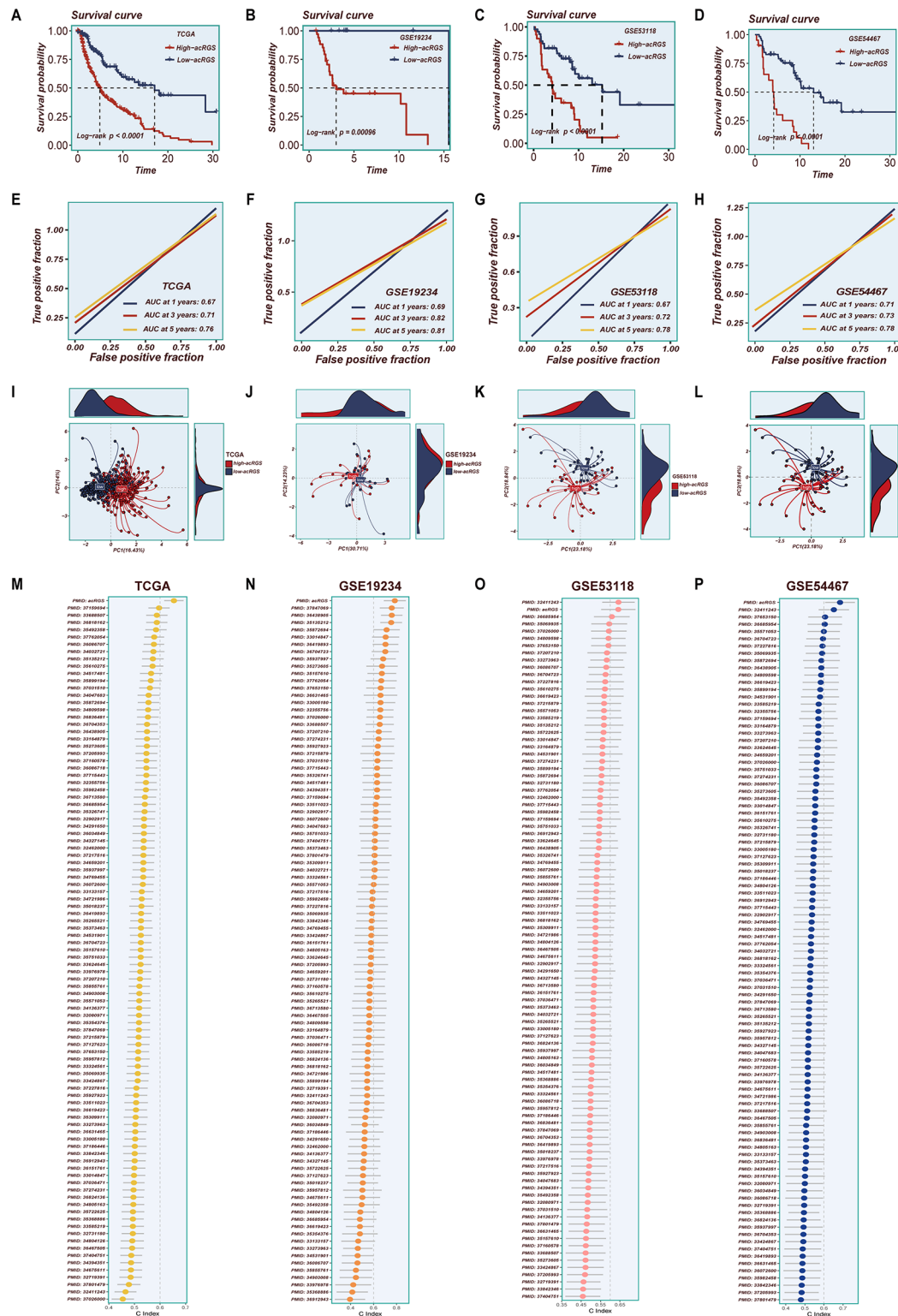
Fig. 5 Assessing and contrasting the predictive value of acRGS in melanoma. (**A**–**D**) Kaplan–Meier curves indicated survival disparities between high- and low-acRGS groups across various cohorts, with the high-acRGS group exhibiting a considerably adverse prognosis. (**E**–**H**) Time-dependent ROC curves of the acRGS for predicting overall survival at 1, 3, and 5 years in the TCGA (**E**), GSE19234 (**F**), GSE53118 (**G**) and GSE54467 (**H**) datasets. (**I**–**L**) Principal component analysis (PCA) of melanoma patients according to the acRGS. (**M**–**P**) Comparison of the C-index between acRGS and 120 published signatures. acRGS indicated superior predictive performance across multiple datasets, achieving the highest C-index value

demonstrated the superior predictive capacity of the acRGS, with AUC values for 1-, 3-, and 5-year OS prediction being 0.67, 0.71, and 0.76 in the training dataset, respectively. Similar values were observed in GSE19234 (0.69, 0.82, and 0.81), GSE53118 (0.67, 0.72, and 0.78), and GSE54467 (0.71, 0.73, and 0.78) (Fig. 5E-H). These results indicate that the acRGS performs consistently across multiple independent cohorts. Additionally, PCA plots from the four datasets demonstrated that acRGS effectively separated patients into two distinct groups (Fig. 5I-L), further confirming its robust discriminatory power in predicting patient outcomes across cohorts. To evaluate the prognostic effectiveness of the acRGS relative to others, we performed a comprehensive review of previously published signatures. These signatures were linked to immune response, autophagy, ferroptosis, epithelial-mesenchymal transition, N6-methyladenosine, and drug sensitivity. Remarkably, the acRGS achieved a higher C-index than many of the existing signatures (Fig. 5M-P), and demonstrated higher accuracy in predicting the prognosis of melanoma patients compared to other clinical features (Fig. S1C). Furthermore, we observed a significant difference in the T stage between the high and low acRGS groups (Fig. S1D), suggesting that the clinical history of melanoma patients may be associated with ac4C modification. Overall, the acRGS proved to be more stable and robust, further highlighting its prognostic value compared to other signatures.

Assessment of tumor immune cell infiltration and immunotherapeutic efficacy based on the acRGS

To validate the clinical applicability of acRGS and minimize bias from the analytical algorithm, we employed seven immune infiltration assessment methods to determine immune cell infiltration in our cohort. As expected, higher infiltration degrees of CD4 + T cells, CD8 + T cells, B cells and macrophages were observed in the high-acRGS subgroup relative to the low-acRGS category (Fig. 6A). Consistent with previous findings, the low-acRGS category revealed elevated levels of immune cell infiltration and immune modulators (Fig. 6B). Besides, the expression of 47 ICGs was investigated, revealing that the majority of ICGs were considerably elevated in the low-acRGS group (Fig. 6C, D). Additionally, correlations between four TME-related scores and acRGS score were evaluated. A considerable negative association was identified between the acRGS score and the stromal score, immune score, and ESTIMATE score, while a positive correlation was noted with tumor purity (Fig. 6E). TCIA scores were applied to assess the potential efficacy of immunotherapy in both groups. The results indicated that the TCIA scores were elevated in the low-acRGS category, implying this cohort has a strong immune subtype and greater responsiveness to

immunotherapy (Fig. 6F). To further evaluate the efficacy of acRGS on immunotherapeutic benefit prediction, we employed our model to two real-world immunotherapy cohorts (anti-PD-L1 in the IMvigor210 cohort and anti-PD-1 in the GSE78220 cohort). As shown in Fig. S1E, in the IMvigor210 cohort, patients with complete response (CR) and partial response (PR) to anti-PD-L1 therapy had significantly lower acRGS scores compared to those with stable and progressive diseases (SD, PD) ($P < 0.001$). Moreover, patients in the low-acRGS group demonstrated a markedly higher frequency of therapeutic benefits compared to the high-acRGS group (36% versus 10%). In addition, the survival time of the high-acRGS group was significantly shorter than that of the low-acRGS group ($P < 0.001$). Similarly, in the GSE78220 cohort, patients who responded to anti-PD-1 demonstrated lower acRGS scores, and the frequency of CR/PR was also notably greater in the low-acRGS group (62% versus 43%) (Fig. S1F). These results suggested that melanoma patients in the low-acRGS group might be sensitivity to immunotherapy.

Multi-omics analysis of acRGS in melanoma

To characterize genomic alterations across melanoma subtypes, we compared somatic mutation frequencies and CNVs between two acRGS groups. As illustrated in Fig. 7A, distinct chromosomal changes were identified, with specific genomic regions displaying notable alterations. The heatmap illustrates the mutation burden in both groups, revealing a markedly higher TMB in the low-acRGS subgroup and acRGS score was negative correlated with TMB (Fig. 7B-D). Additionally, the top twenty genes with the highest mutation frequencies are presented in Fig. 7B. Survival analysis indicated that patients in the high-TMB group experienced favorable outcomes, while those in the low-TMB subgroup confronted worse clinical outcomes (Fig. 7E). When TMB was analyzed in combination with the acRGS score, it was evident that the low-TMB + high-acRGS subgroup exhibited the poorest prognosis, whereas the high-TMB + low-acRGS subgroup demonstrated the most favorable outcomes (Fig. 7F). These findings underscore the synergistic impact of TMB and acRGS score on patients' outcome in melanoma.

Enrichment analysis

As described above, given the upregulated immune-related characteristics in the low-acRGS group, we explored the underlying biological mechanisms. Key steps of the cancer immunity cycle—such as antigen release, priming and activation, immune cell recruitment and infiltration, cancer cell recognition, and cytotoxic killing—were more active in the low-acRGS group. These steps exhibited a significant positive correlation with the
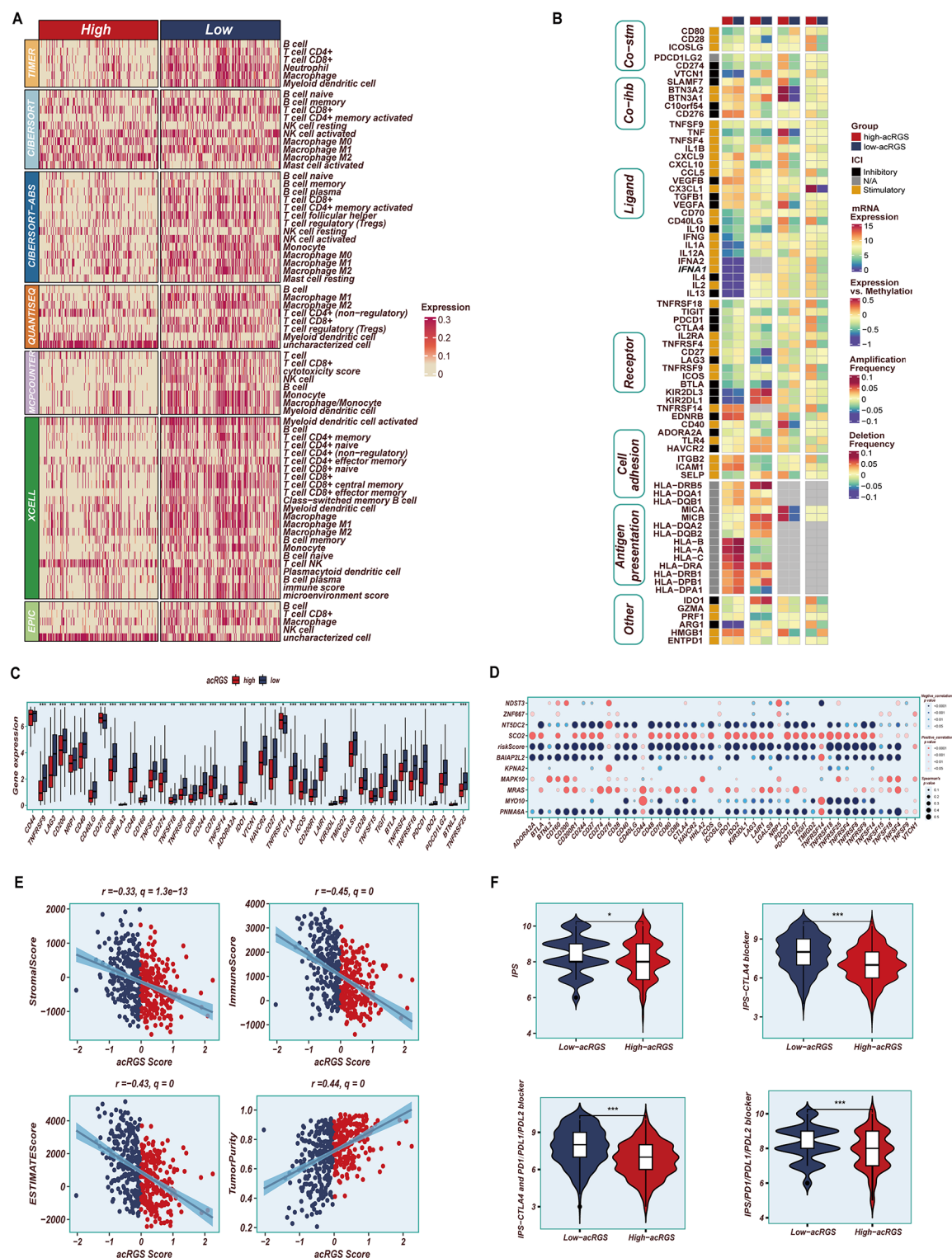
Fig. 6 The landscape of tumor microenvironment (TME) in different acRGS groups. (**A**) The heatmap explicitly illustrates the variations in immune cell infiltration within acRGS groups as assessed through seven predictive algorithms. The z-values represent the relative abundance of immune cell infiltration, clearly suggesting a heightened level of immunological infiltration in the low-acRGS group. (**B**) The heatmap reveals the varying degrees of connections between acRGS groups and immunomodulators. (**C**) The comparison of ICGs expression in the two acRGS groups indicates elevated levels of ICGs expression in the low-acRGS group. (**D**) The bubble plot shows the comparative expression levels of ICGs and acRGS modeling genes. (**E**) Correlations among acRGS score and stromal, immune, and ESTIMATE scores indicate a negative association with immune and stromal score while exhibiting a positive correlation with tumor purity. (**F**) The efficacy of acRGS in predicting the success of immunotherapy
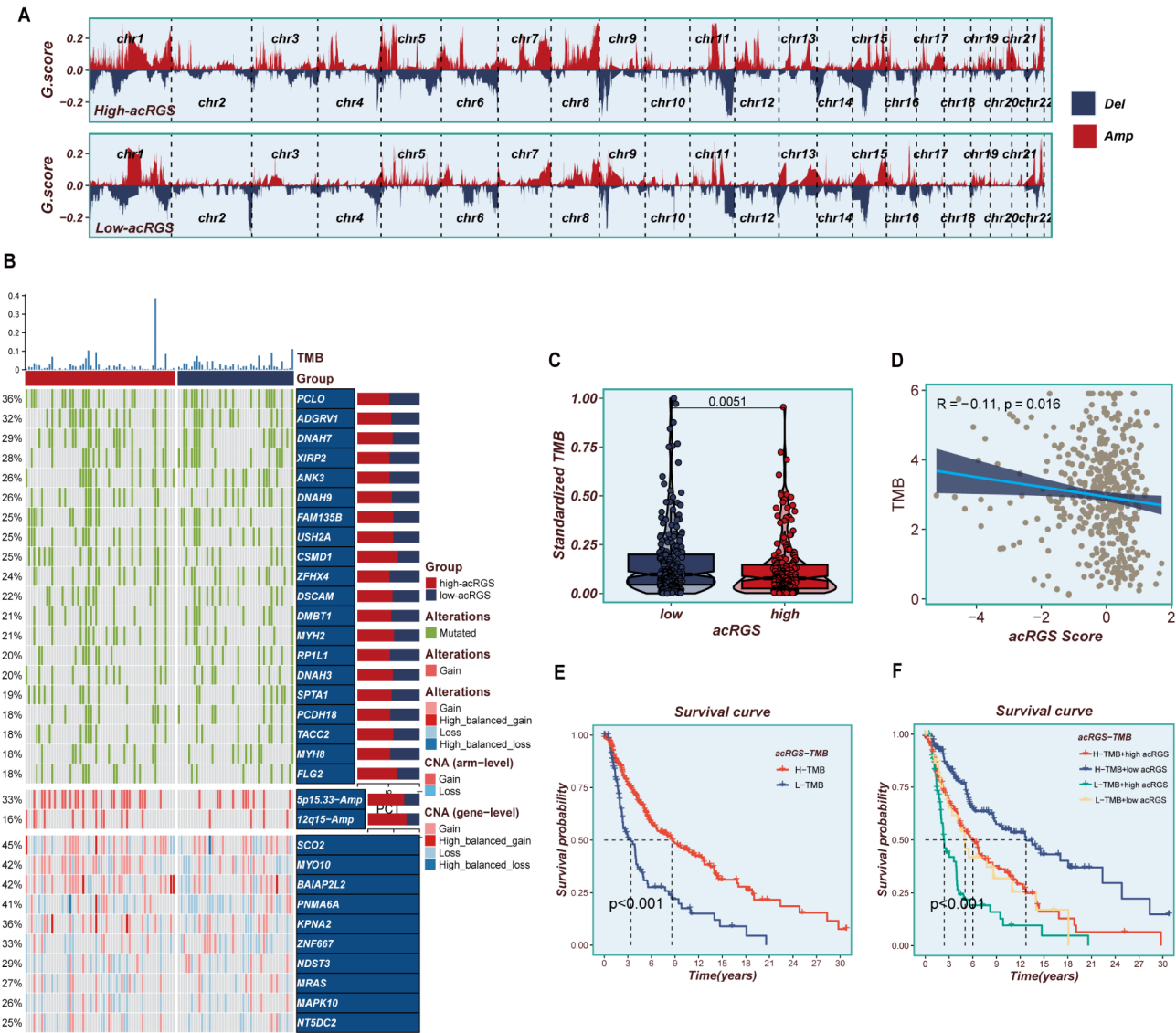
Fig. 7 Genomic and transcriptomic characterization of acRGS in the TCGA cohort. (**A**) Analysis of chromosomal amplifications and deletions in high versus low acRGS groups utilizing GISTIC 2.0. (**B**) Differences in tumor mutation burden (TMB) and genomic alteration profiles between high-acRGS and low-acRGS groups. (**C**, **D**) There existed a notable disparity between the acRGS score and TMB. (**E-F**) Survival analysis across four subgroups delineated by acRGS and TMB revealed divergent prognostic outcomes. The prognosis was markedly poorer in the low-TMB group (**E**). The low-TMB + high-acRGS group exhibited the poorest prognosis, whereas the high-TMB + low-acRGS group demonstrated the most favorable prognosis (**F**)

recruitment of B cells, CD4$^+$T cells, CD8$^+$T cells, and neutrophils, along with the activation of various signaling pathways, including mismatch repair, cell cycle regulation, and DNA replication, as depicted in Fig. 8A. GSVA further demonstrated that acRGS score were associated with both tumorigenic and immunomodulatory pathways. Specifically, acRGS was positively correlated with oncogenic pathways such as E2F targets and the G2M checkpoint, while displaying a strong negative correlation with immunologic pathways, including inflammatory response, T cell-mediated immunity, immune activation, and antigen processing and presentation (Fig. 8B). This may be attributed to acRG activity is highly expressed

in melanocytes, fibroblasts, and endothelial cells. Given that these three cell types exhibit differences in their cell cycle phase percentages, it is likely that acRGS regulates cell cycle-related pathways, which in turn contributes to its association with oncogenic and immune-related pathways. Significant differences in tumorigenic and immunologic pathways were observed between the two acRGS groups (Fig. 8C). Collectively, these findings suggest that low acRGS score is indicative of a stronger immune response, particularly in the context of immunotherapy.
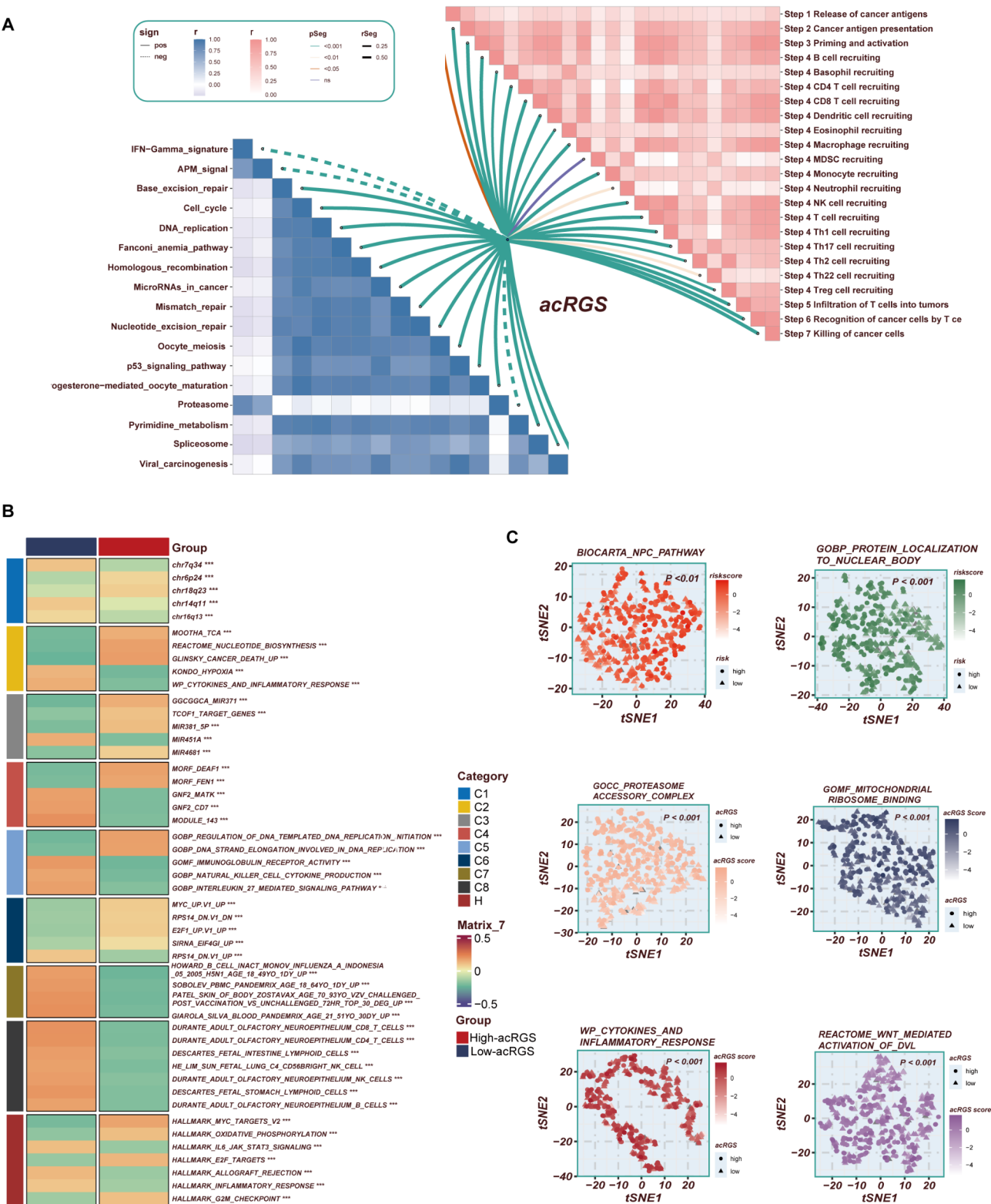
Fig. 8 Biological characterization of acRGS in melanoma. (**A**) The correlation of acRGS with the steps of the cancer immunity cycle (right) and the expression of immune cells (left). (**B**) MsigDB-based GSVA analysis delineated the biological features of two acRGS groups. (**C**) t-SNE visualization of pathway activity disparity between acRGS groups, evaluated through GO and KEGG pathways

Differential analysis of MYO10: prognostic impact and functional annotation

As previously mentioned, our identification of key candidate genes in melanoma holds significant implications in the context of ac4C modification. including MYO10, ZNF667, MRAS, SCO2, MAPK10, PNMA6A, KPNA2, NT5DC2, BAIAP2L2 and NDST3. Among these, MYO10, demonstrating the strongest correlation with the acRGS score, was chosen for further validation as a critical gene (Fig. 9A). Besides, patients exhibiting elevated MYO10 expression in melanoma had worse OS relative to those with reduced MYO10 expression, as depicted in Fig. 9B. Univariate Cox regression analysis confirmed a notable association between MYO10 expression and OS, not only in the TCGA cohort but also across other datasets, including GSE54467, GSE22153 and GSE46517, as depicted in Fig. 9C. The relationships among the MYO10 expression and the abundance of infiltrating immune cells as well as immunomodulators were explored using the BEST database (Fig. 9D, E). Additionally, MYO10 expression was found to have predictive value for both drug resistance and sensitivity to various therapies, as depicted in Fig. 9F. These findings suggest that MYO10 expression exerts a profound impact on melanoma, affecting both patient prognosis and drug responses.

MYO10 downregulation inhibits melanoma progression both in cellular phenotyping and animal assays

To Figure out the biological mechanisms underlying the differences between melanoma and normal tissues, a series of assays were performed. MYO10 mRNA level was considerably elevated in clinical melanoma specimens relative to paired normal tissues, corroborating prior database analysis (Fig. 10A). Similarly, elevated MYO10 expression was noted in melanoma cell lines in comparison to HaCaT cells (Fig. S2A). In an unpublished study, we constructed NAT10-knockdown melanoma cells and performed acRIP-seq analysis. The results revealed an increase in ac4C abundance in MYO10 following NAT10 knockdown, aligning with sequencing data reported in previous studies [9, 34]. Based on these findings, we hypothesized that MYO10 expression is regulated by NAT10-mediated ac4C modification. To test this hypothesis, we conducted ac4C-RIP-qPCR assays, which confirmed an increased ac4C level in MYO10 within melanoma cells compared to normal cells (Fig. S2B). To further investigate the expression level of MYO10 at the melanoma protein level, we analyzed the immunohistochemistry results from the HPA database and observed that MYO10 demonstrated moderate to intense membranous and cytoplasmic staining in melanoma relative to normal skin tissue (Fig. S2C-F). Subsequently, to assess MYO10's functional roles in melanoma cells, A375 and

SK-Mel-28 were treated with shMYO10 lentiviral vectors, and knockdown efficiency was validated by qRT-PCR, revealing a substantial decrease in MYO10 expression following sh-MYO10 transfection (Fig. 10B). Proliferation experiments indicated that MYO10 knockdown markedly suppressed cell viability and colony formation in melanoma cells (Fig. 10C-G). Wound healing assays also exhibited a substantial reduction in wound closure rates following MYO10 silencing (Fig. 10H, I). Moreover, Transwell migration and invasion assays revealed a notable impairment in the migratory and invasive capabilities of MYO10-silenced cells (Fig. 10J, K). To investigate the effect of MYO10 expression on tumor growth in vivo, we constructed a mice subcutaneous xenograft tumor model, and observed that the tumor weight and volume were also drastically decreased due to MYO10 silencing (Fig. 10L-N). Collectively, these findings suggest that MYO10 promotes melanoma progression.

Discussion

RNA acetylation, particularly NAT10-mediated ac4C modification, has made significant advancements in epigenetics, providing a foundation for understanding its role in carcinogenesis and introducing a novel approach to RNA modification [35]. As previously described, ac4C modification is involved in diverse physiological and pathological processes, encompassing cell proliferation, metastasis, lipid metabolism, drug resistance, ferroptosis and apoptosis, by affecting mRNA stability and translation, thereby contributing to cancer progression [11]. For example, NAT10-mediated ac4C modification enhances cervical cancer cell proliferation by stabilizing and modulating the translation of FUS and POLR2A mRNA; [36] while in gastric cancer, it promotes metastasis and epithelial-mesenchymal transition (EMT) by stabilizing COL5A1 mRNA [37]. Furthermore, NAT10 plays a critical role in mitochondrial fatty acid metabolism by modulating ECHS1 and MECR mRNA expression in colon and breast cancers [11]. Given its widespread presence, ac4C modification holds considerable promise as a target for cancer diagnostics and treatment. While this modification appears dynamic and reversible, many regulatory mechanisms remain to be fully elucidated. With regard to other RNA modifications like m6A, m1A, and m5C, the specific role of ac4C in melanoma is still largely unexplored, highlighting the need for further investigation into its therapeutic implications.

In this study, scRNA-seq identified distinct cell clusters within melanoma, including melanocytes, T cells, endothelial cells, fibroblasts and B cells, underscoring the complexity of the TME. Notably, the analysis of acRG activation across these cell types revealed significant variability, with melanocytes displaying markedly higher ac4C modification compared to B and T
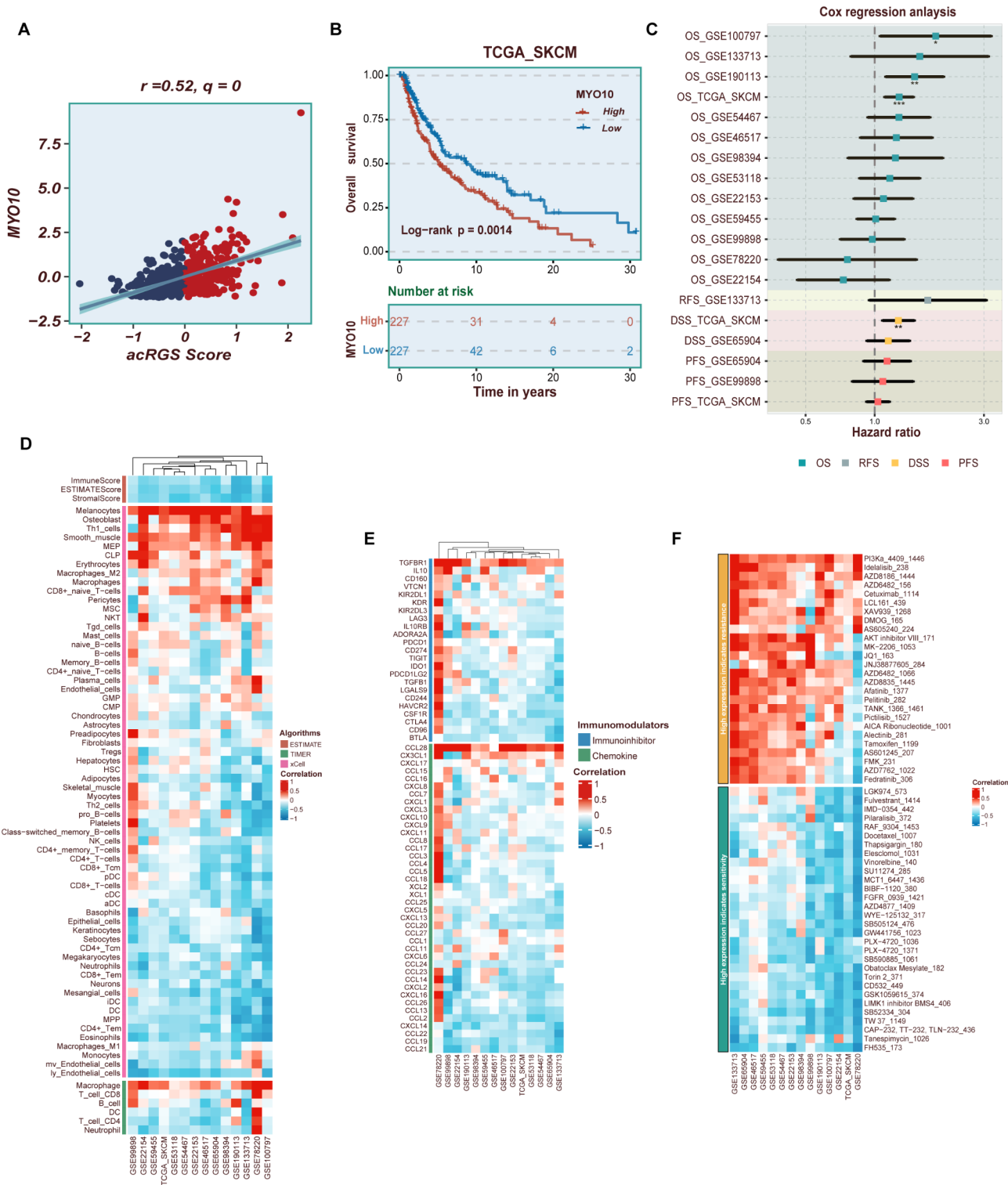
Fig. 9 Exploring the prognostic value of the critical gene MYO10 in melanoma. (**A**) The scatterplot illustrates the correlation between the acRGS score and MYO10 expression in melanoma (*r* = 0.52). (**B**) Assessment of MYO10 as a prognostic factor in melanoma. Patients exhibiting elevated MYO10 expression experienced negative clinical outcomes. (**C**) Univariate Cox regression analysis was conducted across multiple datasets. (**D**) The heatmap highlights the relationship between MYO10 expression and immune cell infiltration across various datasets. (**E**) Correlation between MYO10 expression levels and immunomodulators across several datasets. (**F**) Elevated MYO10 expression forecasts medication responsiveness in melanoma
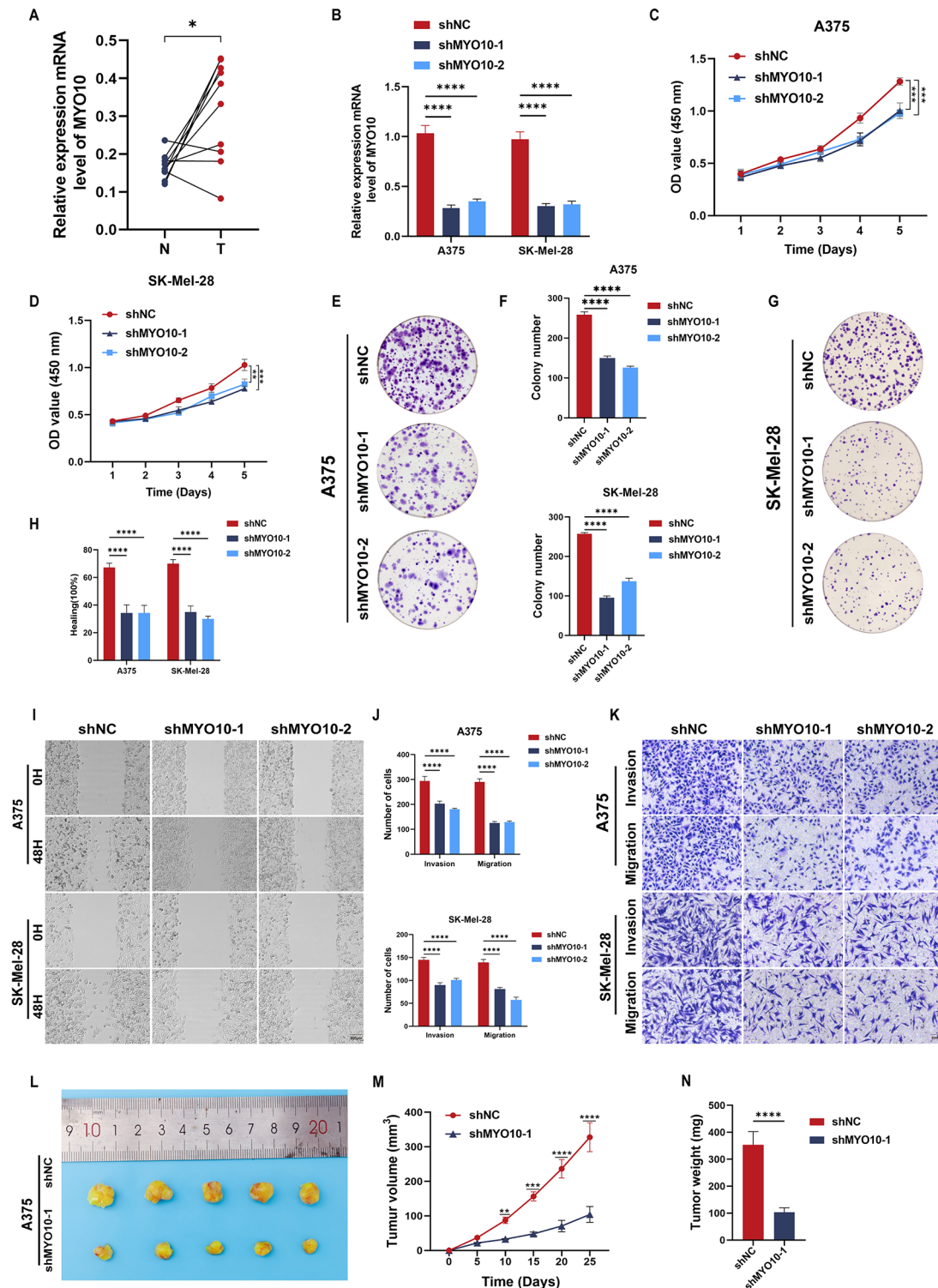
Fig. 10 MYO10 downregulation inhibits melanoma progression both in vitro and in vivo. (**A**) The mRNA levels of MYO10 in ten pairs of melanoma and corresponding normal skin tissues are presented as (T/N). (**B**) QRT-PCR examined the efficacy of MYO10 inhibition. (**C, D**) CCK-8 assays demonstrated that MYO10 inhibition reduced the proliferative capacity of melanoma cells in vitro. (**E–G**) Colony formation assay exhibited a significant reduction in colonies number in the shMYO10 group. (**H, I**) Scratch-wound healing assay indicated significantly slower cell migration after MYO10 knockdown (scale bar, 200 μm). (**J, K**) Transwell assay revealed that downregulation of MYO10 expression impeded the migratory and invasive capacity of melanoma cells (scale bar, 200 μm). (**L**) Representative images of subcutaneous xenograft tumors ($n = 5$ per group). (**M, N**) The growth curves were established by measuring tumor volumes every five days, and the tumor weights were measured. Silencing of MYO10 expression markedly suppressed melanoma cell growth in nude mice. Note: ****$P \leq 0.0001$.***$P \leq 0.001$. **$P \leq 0.01$

cells. Melanocytes accounted for over 60% of the identified cell types, suggesting that an uneven distribution of ac4C modification across the TME. The strong association between acRG and melanocytes prompted further investigation into the role of acRG in melanoma using bulk transcriptome data. ML has emerged as a powerful tool for deriving valuable insights from large datasets. We developed acRGS using 101 different combinations of ML algorithms, which demonstrated exceptional accuracy in predicting OS and outperformed all previously published prognostic signatures. Validation across three independent cohorts further confirmed the superior predictive performance of acRGS, highlighting its potential for future clinical applications.

Immunotherapy has revolutionized the treatment landscape for melanoma, with immune checkpoint inhibitors (ICIs) targeting PD-1, PD-L1, CTLA4, and LAG3 playing a critical role by disrupting signaling pathways that help tumors evade immune surveillance. While melanoma patients who respond favorably to ICIs often experience improved prognoses, not all patients derive lasting benefits, which exemplifies the need for precise identification of those who could benefit from ICIs. Notably, our analysis revealed distinct immune status between the two acRGS groups. The low-acRGS cohort exhibited higher levels of immune infiltrating cells, immune modulators, and biomarkers associated with TME. Furthermore, low acRGS scores were correlated with enhanced activity in the cancer immunity cycle and several immune-related pathways, suggesting its potential value as a predictive biomarker for immunotherapeutic assessment. These findings indicate that acRGS could be a valuable tool for identifying melanoma patients who are more likely to benefit from immunotherapy.

Given the complexity of the immune system, predicting the outcomes of ICIs requires the integration of multiple biomarkers to maximize predictive accuracy. Existing studies have shown that higher TMB is linked to the formation of additional neo-antigens, enhancing tumor immunogenicity and improving clinical responses to immunotherapy [38–40]. Consequently, TMB has emerged as a crucial indicator for predicting immunotherapeutic responsiveness in melanoma [41]. Our investigation revealed a favorable association between elevated TMB levels and improved clinical outcomes. When TMB levels and acRGS score were combined, patients in the high-TMB + low-acRGS group possessed the best prognosis, indicating that integrating acRGS score with TMB levels can accurately identify individuals who are sensitive to immunotherapy.

Through LASSO + StepCox regression, we identified ten genes with irreplaceable prognostic relevance for melanoma: MYO10, ZNF667, MRAS, SCO2, MAPK10, PNMA6A, KPNA2, NT5DC2, BAIAP2L2 and NDST3.

These associations of these genes with other malignancies provides a valuable foundation for exploring their functional roles in melanoma. MYO10, which exhibited the highest hazard ratio (HR), was selected for further validation. As one of several actin-based motor proteins in the myosin superfamily, MYO10 is localized at the tips of filopodia, which are actin-rich, finger-like protrusions at the leading edge of cells, implicated in critical cellular processes such as migration, wound healing, extracellular matrix adhesion, and chemoattractant-guided movement [42, 43]. Recent studies have increasingly highlighted the role of MYO10 in cancer progression. Elevated MYO10 expression has been associated with increased aggressiveness and metastasis in breast cancer [44], while its upregulation has been implicated in lung adenocarcinoma metastasis [45]. MYO10 has also been identified as a target of microRNA-124, which is downregulated in aggressive non-small cell lung cancer [46], and microRNA-340, which suppresses breast cancer metastasis [47]. Additionally, MYO10 expression is significantly higher in prostate cancer compared to normal tissue, where it influences cell migration speed and directional persistence [48]. Previous studies have shown that MYO10 knockout (MYO10ko) mice exhibit abdominal leukoplakia, while MYO10 knockdown (MYO10kd) reduced long protrusion formation and impaired cell migration in cultured melanoblasts. Based on these mice models, it has been proposed that MYO10-driven protrusions play a key role in melanocyte migration, contributing to melanoma initiation and metastasis [49]. This conclusion aligns with our findings. By integrating clinical melanoma samples, cell lines, and both in vivo and in vitro experiments, we identified MYO10 as not only a critical prognostic marker associated with ac4C modification but also a promising therapeutic target for melanoma treatment. In future studies, we aim to elucidate further the precise mechanisms by which MYO10 contributes to melanoma progression, which will be critical for developing targeted therapeutic strategies.

The acRGS developed in this study demonstrated strong immune-related features and significant correlations with patient prognosis, underscoring its potential as a biomarker in clinical practice. However, several limitations should be acknowledged. First, our research integrates acral melanoma and cutaneous melanoma, as both originate from melanocytes, exhibit similar histological features during malignant transformation, and share clinical treatment strategies, to reflect the activity of ac4C modification at the single-cell level. In the future, contingent upon the availability of appropriate datasets, we will perform distinct studies for each subtype. Secondly, the list of acRG may be partial, which could introduce bias. Thirdly, although MYO10's expression and biological function were explored, additional experimental

studies are required to elucidate the specific mechanisms of how MYO10 influences melanoma cell proliferation and migration. Additionally, the prognostic value of the acRGS requires validation in larger and multicenter cohorts.

Conclusions

Through comprehensive analysis of bulk transcriptome and scRNA-seq in melanoma using an innovative mathematical framework and 101 ML algorithms, we developed the acRGS with strong predictive power for distinguishing outcomes in melanoma patients, which not only elucidates the intricate relationship between melanoma heterogeneity and epigenetics but also offers a promising platform for enhancing decision-making and surveillance strategies tailored to individual patients. We expect that this well-organized data will facilitate future clinical investigations and laboratory research to investigate the practical applications and underlying mechanisms of ac4C modification in melanoma.

Abbreviations

ac4C	N4-acetylcytidine
acRG	ac4C-related genes
acRGS	acRG-related signature
OS	Overall survival
CTLA4	Cytotoxic T lymphocyte-associated protein 4
PD-1	Programmed cell death protein 1
tRNA	transfer RNA
rRNA	ribosomal RNA
NAT10	N-acetyltransferase 10
scRNA-seq	single-cell RNA sequencing
DEGs	Differentially expressed genes
ML	Machine learning
GEO	Gene Expression Omnibus database
TCGA	The Cancer Genome Atlas
GTEX	Genotype-Tissue Expression
PCA	Principal component analysis
TPM	Transcripts per million
UMAP	Uniform manifold approximation and projection
GO	Gene ontology
BP	Biological process
KEGG	Kyoto Encyclopedia of Genes and Genomes
RSF	Random survival forest
Enet	Elastic network
SuperPC	Supervised principal components
plsRcox	partial least squares regression for Cox
GBM	Generalized boosted regression modeling
survival-SVM	survival support vector machine
LOOCV	Leave-one-out cross-validation
C-index	Concordance index
KM	Kaplan-Meier
ROC	Receiver operating characteristic
AUC	Area under the curve
CNV	Copy number variation
TMB	Tumor mutation burden
TME	Tumor microenvironment
ssGSEA	single-sample gene set enrichment analysis
ICGs	Immune checkpoint genes
ICIs	Immune checkpoint inhibitors
TCIA	The Cancer Immunome Atlas
GSVA	Gene set variation analysis
HPA	Human Protein Atlas
HaCaT	Human keratinocytes
FBS	Fetal bovine serum
shRNA	short hairpin RNA
ac4C-RIP-seq	ac4C RNA immunoprecipitation sequencing
qRT-PCR	quantitative real-time polymerase chain reaction
CCK-8	Cell counting kit-8
PBS	Phosphate buffer saline
SD	Standard deviation

Supplementary Information

The online version contains supplementary material available at https://doi.org/10.1186/s12967-025-06297-6.

Supplementary Material 1

Supplementary Material 2

Supplementary Material 3

Supplementary Material 4

Declarations

Ethics approval and consent to participate
This study was performed in line with the principles of the Declaration of Helsinki. Approval was granted by the Ethics Committee of the First Affiliated Hospital of Nanjing Medical University (30 August 2022/ No.2022-SR-465). Informed consent has been obtained from all participants involved in the study. All animal procedures adhered to the ethical guidelines of the Animal Experiments Committee at Nanjing Medical University (IACUC-2403031).

Consent for publication
Consent to publish was obtained from the study participants.

Competing interests
The authors declare that they have no competing interests.

Author details
[1]Department of Orthopedics, The First Affiliated Hospital of Nanjing Medical University, Nanjing, China
[2]Department of Lung Cancer, Tianjin Lung Cancer Center, Key Laboratory of Cancer Prevention and Therapy, National Clinical Research Center for Cancer, Tianjin's Clinical Research Center for Cancer, Tianjin Medical University Cancer Institute and Hospital, Tianjin, China
[3]Department of Plastic and Burns Surgery, The First Affiliated Hospital of Nanjing Medical University, Nanjing, China

Liu *et al. Journal of Translational Medicine*   (2025) 23:287

Page 20 of 21

References

1. Love NR, Williams C, Killingbeck EE, Merleev A, Saffari Doost M, Yu L, McPherson JD, Mori H, Borowsky AD, Maverakis E, et al. Melanoma progression and prognostic models drawn from single-cell, Spatial maps of benign and malignant tumors. Sci Adv. 2024;10(28):eadm8206.
2. Long GV, Swetter SM, Menzies AM, Gershenwald JE, Scolyer RA. Cutaneous melanoma. Lancet. 2023;402(10400):485–502.
3. Lv J, Dai B, Kong Y, Shen X, Kong J. Acral melanoma in Chinese: A clinico-pathological and prognostic study of 142 cases. Sci Rep. 2016;6:31432.
4. Lim SY, Rizos H. Single-cell RNA sequencing in melanoma: what have we learned so far? EBioMedicine. 2024;100:104969.
5. Ascierto PA, Dréno B, Larkin J, Ribas A, Liszkay G, Maio M, Mandalà M, Demidov L, Stroyakovskiy D, Thomas L, et al. 5-Year outcomes with Cobimetinib plus Vemurafenib in BRAFV600 Mutation-Positive advanced melanoma: extended Follow-up of the cobrim study. Clin Cancer Res. 2021;27(19):5225–35.
6. Carlino MS, Larkin J, Long GV. Immune checkpoint inhibitors in melanoma. Lancet. 2021;398(10304):1002–14.
7. Wolchok JD, Chiarion-Sileni V, Gonzalez R, Grob JJ, Rutkowski P, Lao CD, Cowey CL, Schadendorf D, Wagstaff J, Dummer R, et al. Long-Term outcomes with nivolumab plus ipilimumab or nivolumab alone versus ipilimumab in patients with advanced melanoma. J Clin Oncol. 2022;40(2):127–37.
8. Long GV, Weber JS, Infante JR, Kim KB, Daud A, Gonzalez R, Sosman JA, Hamid O, Schuchter L, Cebon J, et al. Overall survival and durable responses in patients with BRAF V600-Mutant metastatic melanoma receiving Dabrafenib combined with Trametinib. J Clin Oncol. 2016;34(8):871–8.
9. Arango D, Sturgill D, Alhusaini N, Dillman AA, Sweet TJ, Hanson G, Hosogane M, Sinclair WR, Nanan KK, Mandler MD, et al. Acetylation of cytidine in mRNA promotes translation efficiency. Cell. 2018;175(7):1872–e18861824.
10. Zhao S, Allis CD, Wang GG. The Language of chromatin modification in human cancers. Nat Rev Cancer. 2021;21(7):413–30.
11. Tao L, Lu Y, Chen Z, Ge L, He J, Peng J, Wang H. RNA ac(4)C modification in cancer biology: from regulatory mechanisms to clinical applications. Sci China Life Sci. 2024;67(4):832–5.
12. Hu Z, Lu Y, Cao J, Lin L, Chen X, Zhou Z, Pu J, Chen G, Ma X, Deng Q, et al. N-acetyltransferase NAT10 controls cell fates via connecting mRNA cytidine acetylation to chromatin signaling. Sci Adv. 2024;10(2):eadh9871.
13. Wang X, Ling R, Peng Y, Qiu W, Chen D. RNPS1 stabilizes NAT10 protein to facilitate translation in cancer via tRNA ac(4)C modification. Int J Oral Sci. 2024;16(1):6.
14. Miao D, Shi J, Lv Q, Tan D, Zhao C, Xiong Z, Zhang X. NAT10-mediated ac(4)C-modified ANKZF1 promotes tumor progression and lymphangiogenesis in clear-cell renal cell carcinoma by attenuating YWHAE-driven cytoplasmic retention of YAP1. Cancer Commun (Lond). 2024;44(3):361–83.
15. Liu H, Xu L, Yue S, Su H, Chen X, Liu Q, Li H, Liang H, Chen X, He J et al. Targeting N4-acetylcytidine suppresses hepatocellular carcinoma progression by repressing eEF2-mediated HMGB2 mRNA translation. Cancer Commun (Lond). 2024;44(9):1018–41.
16. Jin G, Xu M, Zou M, Duan S. The processing, gene regulation, biological functions, and clinical relevance of N4-Acetylcytidine on RNA: A systematic review. Mol Ther Nucleic Acids. 2020;20:13–24.
17. Xie R, Cheng L, Huang M, Huang L, Chen Z, Zhang Q, Li H, Lu J, Wang H, Zhou Q, et al. NAT10 drives cisplatin chemoresistance by enhancing ac4C-Associated DNA repair in bladder Cancer. Cancer Res. 2023;83(10):1666–83.
18. Zhang C, Shen H, Yang T, Li T, Liu X, Wang J, Liao Z, Wei J, Lu J, Liu H, et al. A single-cell analysis reveals tumor heterogeneity and immune environment of acral melanoma. Nat Commun. 2022;13(1):7250.
19. Bogunovic D, O'Neill DW, Belitskaya-Levy I, Vacic V, Yu YL, Adams S, Darvishian F, Berman R, Shapiro R, Pavlick AC, et al. Immune profile and mitotic index of metastatic melanoma lesions enhance clinical staging in predicting patient survival. Proc Natl Acad Sci U S A. 2009;106(48):20429–34.
20. Mann GJ, Pupo GM, Campain AE, Carter CD, Schramm SJ, Pianova S, Gerega SK, De Silva C, Lai K, Wilmott JS, et al. BRAF mutation, NRAS mutation, and the absence of an immune-related expressed gene profile predict poor outcome in patients with stage III melanoma. J Invest Dermatol. 2013;133(2):509–17.
21. Jayawardana K, Schramm SJ, Haydu L, Thompson JF, Scolyer RA, Mann GJ, Müller S, Yang JY. Determination of prognosis in metastatic melanoma through integration of clinico-pathologic, mutation, mRNA, MicroRNA, and protein information. Int J Cancer. 2015;136(4):863–74.
22. Zhang Y, Parmigiani G, Johnson WE. ComBat-seq: batch effect adjustment for RNA-seq count data. NAR Genom Bioinform. 2020;2(3):lqaa078.
23. Fan C, Chen F, Chen Y, Huang L, Wang M, Liu Y, Wang Y, Guo H, Zheng N, Liu Y et al. IrGSEA: the integration of single-cell rank-based gene set enrichment analysis. Brief Bioinform. 2024;25(4).
24. Jin S, Plikus MV, Nie Q. CellChat for systematic analysis of cell-cell communication from single-cell transcriptomics. Nat Protoc. 2025;20(1):180–219.
25. Zhang N, Zhang H, Liu Z, Dai Z, Wu W, Zhou R, Li S, Wang Z, Liang X, Wen J, et al. An artificial intelligence network-guided signature for predicting outcome and immunotherapy response in lung adenocarcinoma patients based on 26 machine learning algorithms. Cell Prolif. 2023;56(4):e13409.
26. Liu Z, Liu L, Weng S, Guo C, Dang Q, Xu H, Wang L, Lu T, Zhang Y, Sun Z, et al. Machine learning-based integration develops an immune-derived LncRNA signature for improving outcomes in colorectal cancer. Nat Commun. 2022;13(1):816.
27. Xie J, Wu D, Zhang P, Zhao S, Qi M. Deciphering cutaneous melanoma prognosis through LDL metabolism: Single-cell transcriptomics analysis via 101 machine learning algorithms. Exp Dermatol. 2024;33(4):e15070.
28. Mayakonda A, Lin DC, Assenov Y, Plass C, Koeffler HP. Maftools: efficient and comprehensive analysis of somatic variants in cancer. Genome Res. 2018;28(11):1747–56.
29. Yoshihara K, Shahmoradgoli M, Martínez E, Vegesna R, Kim H, Torres-Garcia W, Treviño V, Shen H, Laird PW, Levine DA, et al. Inferring tumour purity and stromal and immune cell admixture from expression data. Nat Commun. 2013;4:2612.
30. Mariathasan S, Turley SJ, Nickles D, Castiglioni A, Yuen K, Wang Y, Kadel EE III, Koeppen H, Astarita JL, Cubas R, et al. TGFβ attenuates tumour response to PD-L1 Blockade by contributing to exclusion of T cells. Nature. 2018;554(7693):544–8.
31. Hugo W, Zaretsky JM, Sun L, Song C, Moreno BH, Hu-Lieskovan S, Berent-Maoz B, Pang J, Chmielowski B, Cherry G, et al. Genomic and transcriptomic features of response to Anti-PD-1 therapy in metastatic melanoma. Cell. 2016;165(1):35–44.
32. Liu Z, Liu L, Weng S, Xu H, Xing Z, Ren Y, Ge X, Wang L, Guo C, Li L, et al. BEST: a web application for comprehensive biomarker exploration on large-scale data in solid tumors. J Big Data. 2023;10(1):165.
33. Uhlén M, Björling E, Agaton C, Szigyarto CA, Amini B, Andersen E, Andersson AC, Angelidou P, Asplund A, Asplund C, et al. A human protein atlas for normal and cancer tissues based on antibody proteomics. Mol Cell Proteom. 2005;4(12):1920–32.
34. Liu H, Xu L, Yue S, Su H, Chen X, Liu Q, Li H, Liang H, Chen X, He J, et al. Targeting N4-acetylcytidine suppresses hepatocellular carcinoma progression by repressing eEF2-mediated HMGB2 mRNA translation. Cancer Commun (Lond). 2024;44(9):1018–41.
35. Xie L, Zhong X, Cao W, Liu J, Zu X, Chen L. Mechanisms of NAT10 as ac4C writer in diseases. Mol Ther Nucleic Acids. 2023;32:359–68.
36. Arango D, Sturgill D, Yang R, Kanai T, Bauer P, Roy J, Wang Z, Hosogane M, Schiffers S, Oberdoerffer S. Direct epitranscriptomic regulation of mammalian translation initiation through N4-acetylcytidine. Mol Cell. 2022;82(15):2797–e28142711.
37. Zhang Y, Jing Y, Wang Y, Tang J, Zhu X, Jin WL, Wang Y, Yuan W, Li X, Li X. NAT10 promotes gastric cancer metastasis via N4-acetylated COL5A1. Signal Transduct Target Ther. 2021;6(1):173.
38. Yarchoan M, Hopkins A, Jaffee EM. Tumor mutational burden and response rate to PD-1 Inhibition. N Engl J Med. 2017;377(25):2500–1.
39. Rizvi NA, Hellmann MD, Snyder A, Kvistborg P, Makarov V, Havel JJ, Lee W, Yuan J, Wong P, Ho TS, et al. Cancer immunology. Mutational landscape determines sensitivity to PD-1 Blockade in non-small cell lung cancer. Science. 2015;348(6230):124–8.
40. Zhang Y, Zhang Z. The history and advances in cancer immunotherapy: Understanding the characteristics of tumor-infiltrating immune cells and their therapeutic implications. Cell Mol Immunol. 2020;17(8):807–21.
41. Jiang F, Wu C, Wang M, Wei K, Zhou G, Wang J. Multi-omics analysis of tumor mutation burden combined with immune infiltrates in melanoma. Clin Chim Acta. 2020;511:306–18.
42. Berg JS, Derfler BH, Pennisi CM, Corey DP, Cheney RE. Myosin-X, a novel myosin with pleckstrin homology domains, associates with regions of dynamic actin. J Cell Sci. 2000;113(Pt 19):3439–51.
43. Mattila PK, Lappalainen P. Filopodia: molecular architecture and cellular functions. Nat Rev Mol Cell Biol. 2008;9(6):446–54.
44. Cao R, Chen J, Zhang X, Zhai Y, Qing X, Xing W, Zhang L, Malik YS, Yu H, Zhu X. Elevated expression of myosin X in tumours contributes to breast cancer aggressiveness and metastasis. Br J Cancer. 2014;111(3):539–50.

45. Bidkhori G, Narimani Z, Hosseini Ashtiani S, Moeini A, Nowzari-Dalini A, Masoudi-Nejad A. Reconstruction of an integrated genome-scale co-expression network reveals key modules involved in lung adenocarcinoma. PLoS ONE. 2013;8(7):e67552.

46. Sun Y, Ai X, Shen S, Lu S. NF-κB-mediated miR-124 suppresses metastasis of non-small-cell lung cancer by targeting MYO10. Oncotarget. 2015;6(10):8244–54.

47. Chen CP, Sun ZL, Lu X, Wu WX, Guo WL, Lu JJ, Han C, Huang JQ, Fang Y. MiR-340 suppresses cell migration and invasion by targeting MYO10 in breast cancer. Oncol Rep. 2016;35(2):709–16.

48. Makowska KA, Hughes RE, White KJ, Wells CM, Peckham M. Specific myosins control actin organization, cell morphology, and migration in prostate Cancer cells. Cell Rep. 2015;13(10):2118–25.

49. Tokuo H, Bhawan J, Coluccio LM. Myosin X is required for efficient melanoblast migration and melanoma initiation and metastasis. Sci Rep. 2018;8(1):10449.

Publisher's note